

Negative differential thermal conductance and heat amplification in superconducting hybrid devices

Antonio Fornieri,^{1,*} Giuliano Timossi,¹ Riccardo Bosisio,^{2,1} Paolo Solinas,² and Francesco Giazotto^{1,†}

¹NEST, Istituto Nanoscienze-CNR and Scuola Normale Superiore, I-56127 Pisa, Italy

²SPIN-CNR, Via Dodecaneso 33, Genova I-16146, Italy

We investigate the thermal transport properties of a temperature-biased Josephson tunnel junction composed of two different superconductors. We show that this simple system can provide a large negative differential thermal conductance (NDTC) with a peak-to-valley ratio of ~ 3 in the transmitted electronic heat current. The NDTC is then exploited to outline the caloritronic analogue of the tunnel diode, which can exhibit a modulation of the output temperature as large as 80 mK at a bath temperature of 50 mK. Moreover, this device may work in a regime of thermal hysteresis that can be used to store information as a thermal memory. On the other hand, the NDTC effect offers the opportunity to conceive two different designs of a thermal transistor, which might operate as a thermal switch or as an amplifier/modulator. The latter shows a heat amplification factor > 1 in a 500-mK-wide working region of the gate temperature. After the successful realization of heat interferometers and thermal diodes, this kind of structures would complete the conversion of the most important electronic devices in their thermal counterparts, breaking ground for coherent caloritronics nanocircuits where heat currents can be manipulated at will.

I. INTRODUCTION

In the last decade an increasing interest has grown around the possibility to master thermal currents at the nanoscale with the same degree of accuracy obtained in contemporary electronic devices.¹⁻³ This ability would benefit a great number of nanoscience fields, such as solid state cooling,^{1,4,5} thermal isolation,^{6,7} radiation detection¹ and quantum computing.^{8,9} Although being still in their infancy, emerging fields like coherent caloritronics,^{10,11} phononics and thermal logic² have already demonstrated remarkable results towards the implementation of the thermal counterparts of interferometers,^{10,12,13} diodes^{6,14} and solid-state memory devices.¹⁵ Nevertheless, modern electronics had a phenomenal expansion only after the invention of the transistor,¹⁶ whose thermal analogue remains one of the main goals to achieve the full control of heat currents and to finally realize thermal logic gates.²

Exactly ten years ago, Li and coworkers put forward the first theoretical proposal for a thermal transistor,¹⁷ indicating negative differential thermal conductance (NDTC) as an essential requirement to let the device work as a switch or an amplifier. Here, we show that a simple Josephson junction (JJ) between two different superconductors residing at different temperatures can provide a sizeable NDTC, which may give rise to various remarkable effects, like thermal hysteresis and heat amplification. As a result, we can envision several interesting non-linear devices to master electronic heat currents, including the thermal analogues of tunnel diodes,¹⁸ memories¹⁵ and transistors.¹⁶ The proposed devices could be realized with conventional nanofabrication techniques^{6,10,12,13} and might be immediately exploited in low-temperature solid-state thermal circuits.

II. NDTC IN A TEMPERATURE-BIASED JJ

We shall start, first of all, by considering a JJ consisting of two different superconductors (S_1 and S_2) coupled by a thin

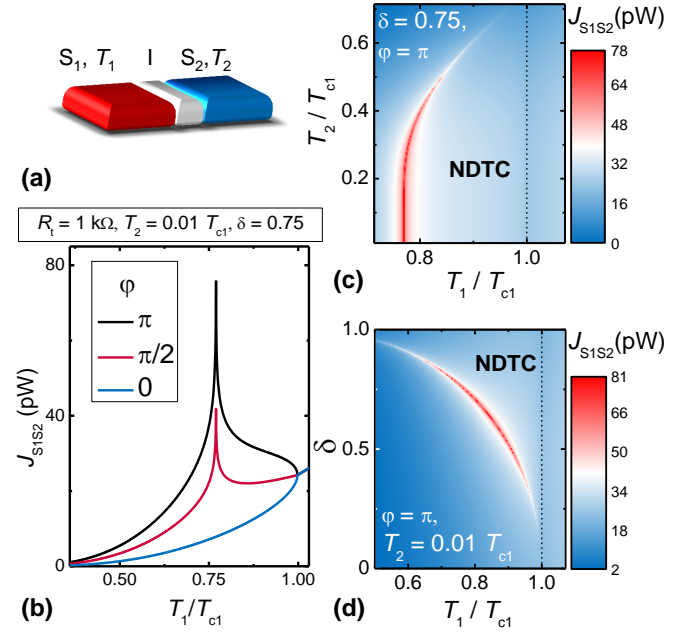


FIG. 1. Thermal transport through a JJ. (a) Schematic configuration of a JJ formed by two superconductors S_1 and S_2 at different temperatures T_1 and T_2 , with $\delta = \Delta_2(0)/\Delta_1(0) \leq 1$. (b) Electronic heat current $J_{S_1S_2}$ vs. T_1 at $T_2 = 0.01T_{c1}$ and for different values of the phase difference ϕ between the superconducting condensates. All the curves are calculated for $\delta = 0.75$. (c) Contour plot showing $J_{S_1S_2}$ as a function of T_1 and T_2 for $\phi = \pi$ and $\delta = 0.75$. (d) Contour plot showing $J_{S_1S_2}$ vs. T_1 and δ for $T_2 = 0.01T_{c1}$ and $\phi = \pi$. In panels (c) and (d) the vertical dashed lines indicate the critical temperature of S_1 . All the results have been obtained by setting the normal-state resistance of the JJ $R_J = 1$ k Ω .

insulating layer (I), as depicted in Fig. 1(a). If we set S_1 at the temperature T_1 and S_2 at T_2 , with $T_1 > T_2$, the electronic heat current flowing through the junction from S_1 to S_2 can be expressed as:²¹⁻²⁵

$$J_{S_1S_2}(T_1, T_2, \phi) = J_{qp}(T_1, T_2) - J_{int}(T_1, T_2) \cos \phi. \quad (1)$$

Here, the first term accounts for the heat carried by quasiparticles, $J_{\text{qp}}(T_1, T_2) = (2/e^2 R_j) \int_0^\infty \varepsilon \mathcal{N}_1(\varepsilon, T_1) \mathcal{N}_2(\varepsilon, T_2) [f(\varepsilon, T_1) - f(\varepsilon, T_2)] d\varepsilon$, where $\mathcal{N}_{1,2}(\varepsilon, T_{1,2}) = |\Re[(\varepsilon + i\Gamma_{1,2})/\sqrt{(\varepsilon + i\Gamma_{1,2})^2 - \Delta_{1,2}^2(T_{1,2})}]|$ are the smeared (if $\Gamma_{1,2} \neq 0$) normalized Bardeen-Cooper-Schrieffer (BCS) densities of states (DOSs) of the superconductors,¹⁹ $f(\varepsilon, T_{1,2}) = [1 + \exp(\varepsilon/k_B T_{1,2})]^{-1}$ is the Fermi-Dirac distribution, $\Delta_{1,2}(T_{1,2})$ are the temperature-dependent energy gaps,²⁰ R_j is the tunnel junction normal-state resistance, e is the electron charge and k_B is the Boltzmann constant. Unless specified otherwise, in the following we will set $\Gamma_{1,2} = \gamma_{1,2} \Delta_{1,2}(0)$, with $\gamma_1 = \gamma_2 = \gamma = 10^{-4}$, which describes realistic superconducting tunnel junctions.^{6,27,28} Furthermore, we shall assume, for clarity, that $\delta = \Delta_2(0)/\Delta_1(0) \leq 1$.

The second component of Eq. (1) stands for the phase-coherent part of the heat current, which originates from energy-carrying tunneling processes involving concomitant destruction and creation of Cooper pairs on different sides of the junction.^{21,22} It is therefore regulated by the phase difference φ between the superconducting condensates and it can be written as $J_{\text{int}}(T_1, T_2) = (2/e^2 R_j) \int_0^\infty \varepsilon \mathcal{M}_1(\varepsilon, T_1) \mathcal{M}_2(\varepsilon, T_2) [f(\varepsilon, T_1) - f(\varepsilon, T_2)] d\varepsilon$ (Ref. 25), where $\mathcal{M}_{1,2}(\varepsilon, T_{1,2}) = |\Im[-i\Delta_{1,2}(T_{1,2})/\sqrt{(\varepsilon + i\Gamma_{1,2})^2 - \Delta_{1,2}^2(T_{1,2})}]|$ is the Cooper pair BCS DOSs in the superconductors.²⁶ J_{int} represent the thermal counterpart of the "quasiparticle-pair interference" contribution to the *charge* current tunneling through a JJ.^{26,29-31} Depending on φ , it can flow in opposite direction with respect to that imposed by the thermal gradient, but the total heat current $J_{S_1 S_2}$ still flows from the hot to the cold reservoir, thus preserving the second principle of thermodynamics. This was experimentally demonstrated in Ref. 10.

Figure 1(b) shows the behavior of $J_{S_1 S_2}$ vs. T_1 for $T_2 = 0.01 T_{c1}$ (T_{c1} being the critical temperature of S_1) and $\delta = 0.75$. It appears evident how the variation of φ can strongly influence the thermal transport through the JJ. First, let us focus on the case in which $\varphi = \pi/2$. In this condition, $J_{S_1 S_2}$ becomes equal to J_{qp} , which presents a sharp peak at $T_1 \simeq 0.77 T_{c1}$, due to the matching of singularities in the superconducting DOSs \mathcal{N} when $\Delta_1(T_1) = \Delta_2(T_2)$. At higher values of T_1 , $\Delta_1(T_1) < \Delta_2(T_2)$ and the energy transmission through the junction is reduced, thus originating an effect of NDTC. This feature is the analogue of the well-known singularity-matching peak (SMP) usually observed in the quasiparticle current flowing through a voltage-biased $S_1 I S_2$ junction.²⁶ Yet, in the thermal configuration, the effect of NDTC can be enhanced or reduced by the presence of J_{int} as determined by the value of φ . At $\varphi = 0$ the SMP is perfectly canceled by the coherent component of the heat current, while at $\varphi = \pi$ it becomes almost doubled and an additional NDTC feature appears, owing to the gradual suppression of J_{int} as T_1 approaches T_{c1} . This results in a remarkable peak-to-valley ratio of $\simeq 3.1$. The behaviour of J_{int} is due to the singularity of \mathcal{M} at $\varepsilon = \Delta$ that perfectly corresponds to the one in \mathcal{N} , creating a sort of resonance between quasiparticle and pair tunneling.^{26,30}

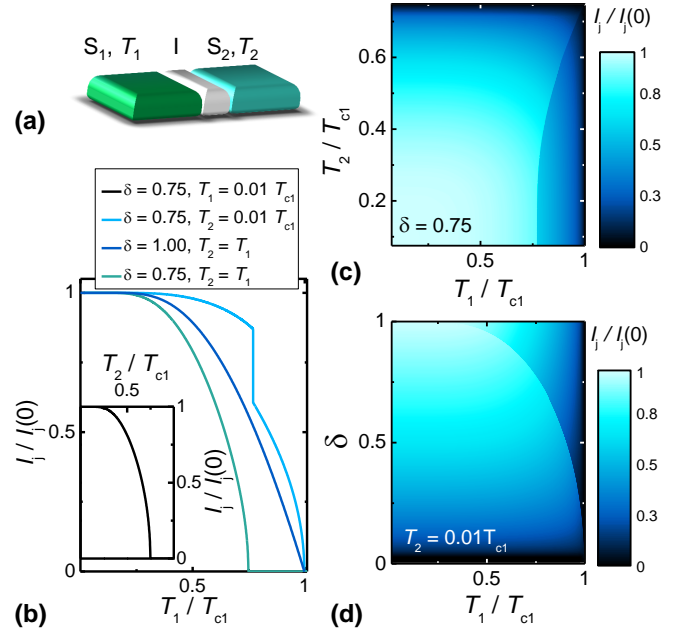


FIG. 2. Non-dissipative charge transport through a JJ. (a) Schematic configuration of the same JJ depicted in Fig. 1(a). (b) Normalized Josephson critical current I_j vs. T_1 for different configurations of T_2 and δ . Inset: I_j as a function of T_2 for $\delta = 0.75$ and $T_1 = 0.01 T_{c1}$. (c) Contour plot showing I_j vs. T_1 and T_2 for $\delta = 0.75$. (d) Contour plot showing I_j vs. T_1 and δ for $T_2 = 0.01 T_{c1}$.

The effect of NDTC depends also on the amplitude of $\Delta_2(T_2)$, as shown in the contour plot of Fig. 1(c). As T_2 is increased, the position of the SMP moves towards higher values of T_1 and its amplitude gradually decreases. It is worth noting that while the NDTC effect extends from the SMP to T_{c1} if we vary T_1 and keep T_2 fixed, it is much more localized in the proximity of the SMP if we vary T_2 and keep T_1 fixed. This will be important to understand the performances of different configurations for a superconducting thermal transistor (see Sect. VIII).

Finally, Fig. 1(d) displays the impact of δ on the region of NDTC. As $\Delta_2(0)$ becomes more similar to $\Delta_1(0)$ the extension of the NDTC region increases to the detriment of its amplitude. Therefore, the best configuration results to be the one with $\delta \simeq 0.75$.

III. BEHAVIOR OF THE JOSEPHSON CURRENT

Before proceeding in the analysis of the possible ways to exploit NDTC, we first consider the electrical behavior of the JJ. The latter, as we shall argue, presents interesting features and can be used to probe the electronic temperature in a superconductor.

The system described in the previous section can support a non-dissipative Josephson current that follows the well-known expression:²⁹

$$I_0(T_1, T_2) = I_j(T_1, T_2) \sin \varphi, \quad (2)$$

where I_j is the critical current of the JJ, which can be evaluated with the generalized Ambegaokar-Baratoff relation:^{32,33}

$$I_j(T_1, T_2) = \frac{1}{2eR_j} \left| \int_{-\infty}^{\infty} d\varepsilon \{ \mathbf{f}(\varepsilon, T_1) \Re[\mathcal{F}_1(\varepsilon, T_1)] \Im[\mathcal{F}_2(\varepsilon, T_2)] + \mathbf{f}(\varepsilon, T_2) \Re[\mathcal{F}_2(\varepsilon, T_2)] \Im[\mathcal{F}_1(\varepsilon, T_1)] \} \right|. \quad (3)$$

Here, $\mathbf{f}(\varepsilon, T_{1,2}) = \tanh(\varepsilon/2k_B T_{1,2})$ and $\mathcal{F}_{1,2}(\varepsilon, T_{1,2}) = \Delta_{1,2} / \sqrt{(\varepsilon + i\Gamma_{1,2})^2 - \Delta_{1,2}^2(T_{1,2})}$ are the anomalous Green's functions in the superconductors.²⁶

Figure 2(b) displays I_j as a function of T_1 for three representative configurations of the JJ. First we consider the case in which no temperature gradient is set across the junction: if $\delta = 1$, we recover the conventional result by Ambegaokar-Baratoff,³⁴ i.e. $I_j = (\pi\Delta/2eR_j)\tanh(\Delta/2k_B T)$ vanishing at T_{c1} with a finite slope. On the other hand, if $\delta < 1$ the critical current goes to zero at T_{c2} with an infinite slope, following the BCS temperature-dependence of Δ_2 . More interestingly, if we fix T_2 and we let only T_1 vary, we obtain a sharp jump of I_j at $T_1 \simeq 0.77T_{c1}$ for $\delta = 0.75$. This feature stems again from the alignment of the singularities in the Green's functions \mathcal{F} at $\varepsilon = \Delta$ when $\Delta_1(T_1) = \Delta_2(T_2)$, and to our knowledge it has never been observed so far. As shown in the inset of Fig. 2(b), if we vary T_2 and keep $T_1 = 0.01T_{c1}$ the critical current decreases monotonically and without jumps, since in this configuration the condition $\Delta_1(T_1) = \Delta_2(T_2)$ is never met. The occurrence of this condition is mapped in the contour plots of Figs. 2(c) and 2(d), which are the equivalent of those shown previously in Figs. 1(c) and 1(d).

The above analysis confirms that a JJ can easily serve as a non-dissipative thermometer for the electronic temperature of a superconducting electrode above $\simeq 0.4T_c$.¹ Since the NDTC effect occurs at temperatures relatively close to the critical one, for our purposes this kind of thermometry would represent a good alternative to more conventional methods, which are focused on the quasiparticle transport.^{1,35}

IV. PHASE-BIAS OF THE JJ

In order to maximize the effect of NDTC, the JJ between S_1 and S_2 (that we will label as j in this section) must be biased at $\varphi = \pi$, as shown in Sect. II. Phase biasing of a JJ can be achieved, in general, through supercurrent injection or by applying an external magnetic flux.³⁶ In our case, the ideal way to obtain a full control over φ is to realize a "fake" radio frequency superconducting quantum interference device (rf SQUID), as depicted in Fig. 3(a). The superconducting electrodes S_1 and S_2 are connected to a third superconductor S_3 (possibly with $\Delta_3(0) > \Delta_1(0), \Delta_2(0)$ so to suppress heat losses) by means of two parallel JJs named a and b . The three superconductors form a loop with three JJs, two of which are in series on the same branch [see Fig. 3(b)]. As we shall argue, in order to obtain a π polarization between S_1 and S_2 , the junction j must be characterized by the lowest Josephson critical current in the SQUID, so that most of the phase drop occurs across this junction.

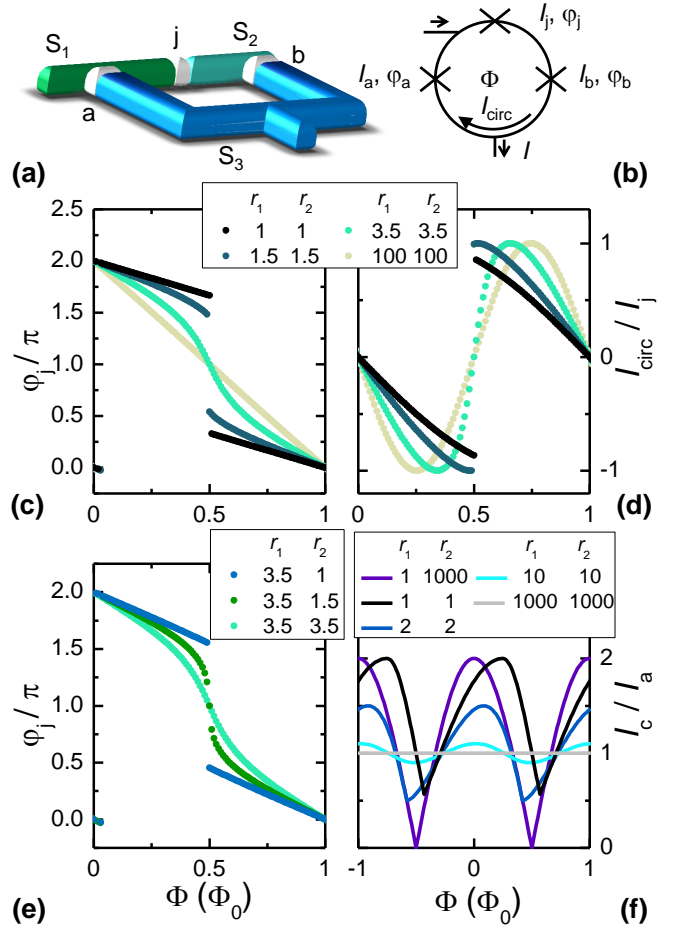


FIG. 3. Phase-biasing a JJ by means of a three-junction SQUID. (a) Pictorial representation of the interferometer. (b) Circuitual scheme of the device. (c) Magnetic-flux dependence of the phase difference φ_j across the junction j for symmetric values of $r_1 = I_a/I_j$ and $r_2 = I_b/I_j$. (d) Normalized circulating current I_{circ} vs. Φ for the same values of r_1 and r_2 displayed in panel (c). (e) Phase polarization of φ_j vs. Φ for asymmetric values of r_1 and r_2 . (f) Magnetic-flux dependence of the normalized SQUID critical current I_c for several combinations of r_1 and r_2 .

The described interferometer is characterized by the following set of equations:

$$\varphi_a - (\varphi_b + \varphi_j) + 2\pi \frac{\Phi}{\Phi_0} = 2n\pi, \quad (4)$$

$$I = I_a \sin \varphi_a + I_b \sin \varphi_b, \quad (5)$$

$$I_j \sin \varphi_j = I_b \sin \varphi_b, \quad (6)$$

$$I_{\text{circ}} = \frac{1}{2} (I_a \sin \varphi_a - I_b \sin \varphi_b), \quad (7)$$

where I_k and φ_k are the Josephson critical current and phase difference for the k -th junction, with $k = a, b, j$, Φ is the external magnetic flux threading the loop, $\Phi_0 \simeq 2 \times 10^{-15}$ is the superconducting flux quantum and n is an integer. Equation (4) establishes the flux-phase quantization along the loop, Eq. (5) expresses the Kirchoff law for the total supercurrent I flowing through the SQUID, Eq. (6) imposes the current conser-

variation in one branch of the interferometer and, finally, Eq. (7) describes the circulating supercurrent I_{circ} .

As we shall explain in the following section, we can phase-bias the thermal transport through junction j by just applying an external magnetic flux piercing the loop of the SQUID. In this configuration, only a circulating supercurrent can flow along the loop and $I = 0$. From Eqs. (4) and (6), we can extract the following expressions for φ_a and φ_b :

$$\varphi_a = (\varphi_b + \varphi_j) + 2\pi \frac{\Phi}{\Phi_0}, \quad (8)$$

$$\varphi_b = (-1)^m \arcsin\left(\frac{1}{r_2} \sin \varphi_j\right) + m\pi, \quad (9)$$

where $r_2 = I_b/I_j$ and $m = 0, 1$. If we substitute Eqs. (8) and (9) into Eq. (5), we obtain two branches of solutions for φ_j depending on m . The correct physical values are those which minimize the Josephson free energy of the system $E_J = E_J^a + E_J^b + E_J^j$, with $E_J^k = (\Phi_0 I_k / 2\pi)(1 - \cos \varphi_k)$.²⁰

Figures 3(c) and 3(d) show the magnetic-flux dependence of φ_j and I_{circ} for different values of r_1 and r_2 , where $r_1 = I_a/I_j$. As r_1 and r_2 increase (i.e. as I_j becomes smaller than I_a, I_b), φ_j is able to reach the values around π more smoothly and the I_{circ} characteristic becomes more sinusoidal, like in a standard rf SQUID. The obtained results reveal that the threshold to obtain a continuous π polarization (without abrupt switches) is $r_1 = r_2 \geq 2.5$. Moreover, if we introduce an asymmetry between I_a and I_b above 40%, the jump in the φ_j polarization curve reappears, as shown in Fig. 3(e). It is also worth noting that when $\varphi_j = \pi$, we have $\varphi_a = \varphi_b = 0$.

To conclude this section, we discuss the magnetic interference pattern of the SQUID total critical current I_c , which represents the simplest measurement to characterize the interferometer. To obtain $I_c(\Phi)$ we substitute again Eqs. (8) and (9) into Eq. (5) and we maximize the value of I with respect to φ_j . As previously mentioned, the correct solution is the one corresponding to the minimum of the Josephson energy. The resulting behavior of I_c vs. Φ is shown in Fig. 3(d), where we recognize three limit cases: first, if $(r_1, r_2) = (1, 1000)$, i.e. $I_b \gg I_{a,j}$, the junction b becomes almost completely transparent, leaving just the junctions a and j to define a symmetric direct-current SQUID with the conventional pattern $\propto |\cos(\pi\Phi/\Phi_0)|$. On the other hand, if $(r_1, r_2) = (1, 1)$, that is $I_a = I_b = I_j$, the three-junction SQUID is completely symmetric and I_c presents a skewed pattern that never vanishes. Lastly, when $(r_1, r_2) = (1000, 1000)$, i.e. $I_a = I_b \gg I_j$, the junctions a and b become almost transparent with respect to junction j, thus forming a true rf SQUID. The latter is characterized by an almost constant I_c , since the branch with only the transparent junction a shunts the circuit. We also notice that for $(r_1, r_2) \geq (2.5, 2.5)$ the I_c characteristic loses the cusped minima and progressively turns into a sinusoid with reduced contrast.

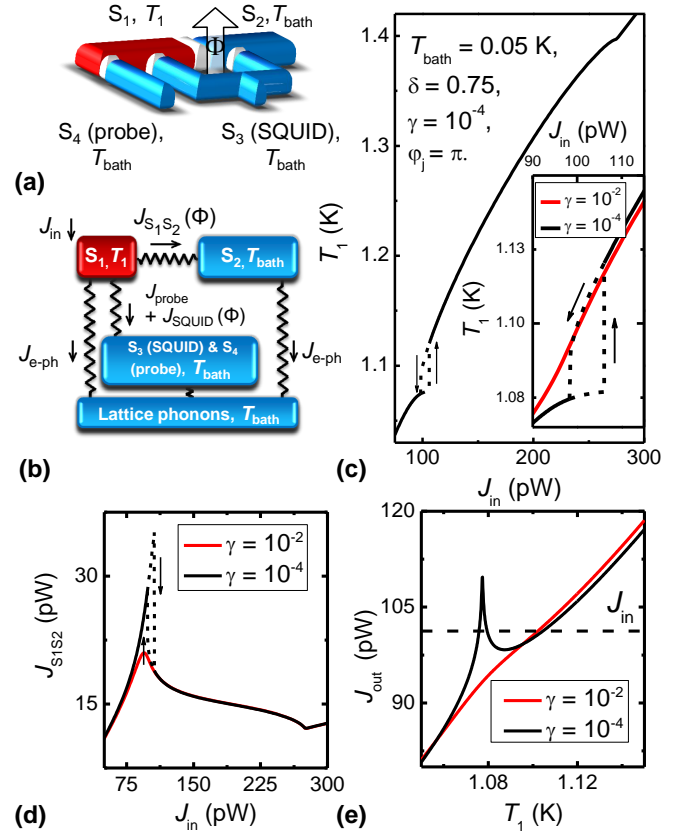


FIG. 4. Performance of the tunnel heat diode (design 1). (a) Pictorial representation of the device. (b) Thermal model outlining the relevant heat exchange mechanisms present in our tunnel diode. Arrows indicate heat current directions for the operating device, that is, when $T_1 > T_{\text{bath}}$ (see text). (c) Calculated electronic temperature T_1 vs. the injected power J_{in} for $\gamma = 10^{-4}$. Inset: zoom of the hysteretic region of T_1 for two values of γ . The arrows near the curves indicate the J_{in} sweep direction. (d) Electronic heat current $J_{S_1S_2}$ vs. J_{in} for two values of γ . (e) Input and output heat currents J_{in} (dashed line) and J_{out} (solid line) vs. T_1 for the same values of γ shown in the other panels. All the results have been obtained at a bath temperature $T_{\text{bath}} = 50$ mK and for $\delta = 0.75$, $\varphi_j = \pi$ and $\varphi_a = \varphi_b = 0$. We assumed that S_1, S_3 and S_4 are composed of aluminum with $T_c = 1.4$ K. The normal-state resistances are $R_j = 2$ k Ω and $R_a = R_{\text{probe}} = 500$ Ω , whereas the volume of S_1 is $V_1 = 1 \times 10^{-19}$ m³. For completeness, in the thermal model we also included two superconducting probes tunnel-coupled to S_1 acting as Josephson thermometers (see Sect.III) with a normal-state resistance $R_{\text{thermo}} = 2$ k Ω for each junction (not shown).

V. NDTc AND THERMAL MEMORY IN A HEAT TUNNEL DIODE

We now have all the elements necessary to envision a realistic caloritronic device able to provide a measurable NDTc, i.e. the thermal analogue of the electric tunnel diode. As any direct measurement of the heat current is unfeasible, the design of the thermal tunnel diode must be conceived to manifest sizeable effects in the temperature of the electrodes. The simplest geometry for such a device consists in connecting a superconducting lead S_3 to S_1 and S_2 , forming the three-junction

SQUID described in the previous section [see Fig. 4(a)]. Furthermore, a superconducting probe S_4 tunnel-coupled to S_1 would offer the possibility to investigate the electrical transport through the device (see Sects. III and IV). We emphasize that our analysis is focused on the heat carried by electrons only. We assume that lattice phonons present in every part of our structure are fully thermalized with the substrate phonons residing at the bath temperature T_{bath} , thanks to the vanishing Kapitza resistance between thin metallic films and the substrate at low temperatures.^{6,10,12,13,37} If we inject a Joule power J_{in} into S_1 , we can raise its electronic temperature T_1 significantly above T_{bath} ,³⁷ generating a thermal gradient across the device. This hypothesis is expected to hold because the other electrodes of the tunnel diode (S_2 , S_3 and S_4) can be designed to extend into large-volume leads, providing efficient thermalization of their quasiparticles at T_{bath} . This thermal gradient originates a finite heat current $J_{S_1S_2}$, which displays a remarkable NDTC effect, as shown in Sect. II.

In order to predict the behavior of the heat tunnel diode, we formulate a thermal model accounting for all the predominant heat exchange mechanisms present in the structure. The model is sketched in Fig. 4(b), where J_{SQUID} and J_{probe} are the electronic heat currents flowing from S_1 to S_3 and S_4 , respectively, through two JJs characterized by normal-state resistances R_a and R_{probe} . Furthermore, we take into account the energy relaxation due to the electron-phonon coupling $J_{e\text{-ph}}$, which in a superconductor at temperature T can be expressed as:³⁵

$$J_{e\text{-ph}}(T, T_{\text{bath}}) = -\frac{\Sigma \mathcal{V}}{96\zeta(5)k_{\text{B}}^5} \int_{-\infty}^{\infty} dE E \int_{-\infty}^{\infty} d\varepsilon \varepsilon^2 \text{sgn}(\varepsilon) \\ \times L(E, E + \varepsilon, T) \left\{ \coth\left(\frac{\varepsilon}{2k_{\text{B}}T_{\text{bath}}}\right) \right. \\ \times [\mathbf{f}(E, T) - \mathbf{f}(E + \varepsilon, T)] \\ \left. - \mathbf{f}(E, T)\mathbf{f}(E + \varepsilon, T) + 1 \right\}. \quad (10)$$

Here, Σ is the material-dependent electron-phonon coupling constant, \mathcal{V} is the volume of the superconducting electrode and $L(E, E', T) = \mathcal{N}(E, T)\mathcal{N}(E', T)[1 - \Delta^2(T)/(EE')]$. Therefore, the steady-state electronic temperature T_1 can be calculated as a function of J_{in} by solving the following energy balance equation:

$$J_{\text{in}} = J_{\text{out}} \\ = J_{S_1S_2}(T_1, T_{\text{bath}}) + J_{e\text{-ph}}(T_1, T_{\text{bath}}) \\ + J_{\text{SQUID}}(T_1, T_{\text{bath}}) + J_{\text{probe}}(T_1, T_{\text{bath}}), \quad (11)$$

which imposes that the sum of all the incoming (J_{in}) and outgoing (J_{out}) heat currents for S_1 must be equal to zero. The resulting trend of T_1 vs. J_{in} is shown in Fig. 4(c), where we set $T_{\text{bath}} = 50$ mK, $\delta = 0.75$, $\phi_j = \pi$ and $\phi_a = 0$. The normal-state resistances were designated to be $R_j = 2$ k Ω and $R_a = R_{\text{probe}} = 500$ Ω . We also assumed that S_1 , the SQUID and the probe are composed of aluminum (Al) with $T_c = 1.4$ K and $\Sigma = 3 \times 10^8$ WK⁻⁵m⁻³ (Ref. 1), whereas the volume of S_1 is $\mathcal{V}_1 = 1 \times 10^{-19}$ m³. In order to obtain a proper value of δ , S_2 can be realized as a bilayer of a normal metal in clean

contact with a superconductor: owing to the inverse proximity effect, Δ and T_c can be manipulated at will by varying the thicknesses of the layers.^{38,39}

The calculated results present two prominent features: at $J_{\text{in}} \simeq 100$ pW the slope of T_1 suddenly increases and a region of thermal hysteresis appears [see Fig. 4(c)]. As a matter of fact, the T_1 curve creates a loop instead of retracing its path for increasing and decreasing J_{in} , showing bi-stable temperature states for a given input power. Both the features are indirect evidences of NDTC in $J_{S_1S_2}$, which is displayed in Fig. 4(d). In particular, the increase in the derivative of T_1 corresponds to the onset of the NDTC regime, in which S_1 results to be more isolated from S_2 and gets heated more efficiently by the injection of J_{in} . The end of the NDTC region coincides with the transition of S_1 into a normal metal at 1.4 K, where T_1 shows a cusp. Even more interesting, for small values of γ the SMP in $J_{S_1S_2}$ generates an hysteresis in the T_1 curve, as highlighted in the inset of Fig. 4(c). This effect can be easily understood by plotting J_{in} and J_{out} vs. T_1 , as displayed in Fig. 4(e) with a dashed and a solid line, respectively. In the graph, the intersections between J_{in} and J_{out} are indicating the possible solutions for T_1 . When $\gamma = 10^{-4}$, three solutions are visible for 98 pW $\lesssim J_{\text{in}} \lesssim 106$ pW, of which only two are in the positive slope parts of the J_{out} curve and are hence stable operating points of the device. On the contrary, if γ is increased, the SMP in $J_{S_1S_2}$ becomes broadened [see Fig. 4(d)], J_{out} turns into a monotonic function and Eq. (11) has therefore a single solution for T_1 in the whole range of J_{in} .

The region of thermal hysteresis can be used to realize a thermal memory device, in analogy to what has been done in Ref. 15. Indeed, in this region S_1 can reside at two different temperatures T_{high} and T_{low} for a given J_{in} . These can be considered as the logical Boolean units 1 ($= T_{\text{high}}$) and 0 ($= T_{\text{low}}$) to store and read thermal information on the tunnel diode. In order to perform a cycle of writing and reading, we define $J_{\text{read}} \simeq 102$ pW in the middle of the hysteretic regime [see the inset of Fig. 4(c)], whereas we label $J_{\text{high}} = 110$ pW and $J_{\text{low}} = 95$ pW outside the boundaries of the multi-valued region. In this way, we can write 1 or 0 by setting $J_{\text{in}} = J_{\text{high}}$ or $J_{\text{in}} = J_{\text{low}}$, respectively, and afterward read the stored information by applying $J_{\text{in}} = J_{\text{read}}$. The performance and repeatability of this process is certainly improved if the temperature difference $\delta T = [T_{\text{high}} - T_{\text{low}}]_{J_{\text{in,read}}}$ is maximized, in order to reduce the number of errors caused by noise and fluctuations. For the chosen R_j , $\delta T = 32$ mK, but this value can be increased up to 56 mK by reducing R_j down to 1.1 k Ω (the latter being the minimum normal-state resistance that preserves the π -polarization of ϕ_j).

Finally, we spend a few words about the heat current noise that might affect the proposed system, leading to a reduced visibility of the hysteretic regime. We assume to inject J_{in} by means of two superconducting probes S_5 tunnel-coupled to S_1 in order to form a $S_5IS_1IS_5$ junction.³⁵ If we apply a voltage $V > 2(\Delta_1 + \Delta_5)/e$, we dissipate a Joule power in S_1 , which represents the main source of noise in our system. The noise spectral density associated to J_{in} is detailed in Ref. 40 and can be estimated of the order of $10^{-17} \div 10^{-16}$ W/Hz^{1/2}. In the present setup, the admitted frequency band can extend up to

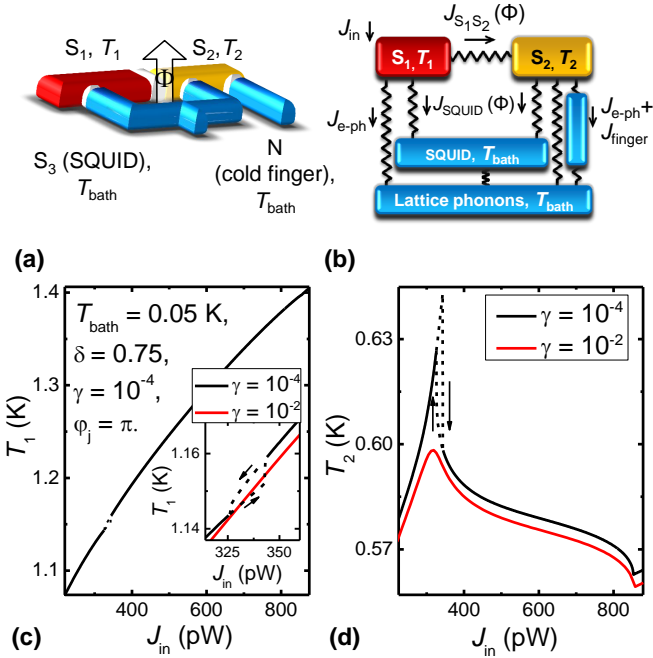


FIG. 5. Performance of the tunnel heat diode (design 2). (a) Pictorial representation of the device. (b) Thermal model outlining the relevant heat exchange mechanisms present in our tunnel diode when $T_1 > T_2 > T_{\text{bath}}$. (c) Calculated electronic temperature T_1 vs. the injected power J_{in} for $\gamma = 10^{-4}$. Inset: zoom of the hysteretic region of T_1 for two values of γ . The arrows near the curves indicate the J_{in} sweep direction. (d) Electronic temperature T_2 vs. J_{in} for the same values of γ shown in the inset of panel (c). All the results have been obtained at a bath temperature $T_{\text{bath}} = 50$ mK and for $\delta = 0.75$, $\varphi_j = \pi$ and $\varphi_a = \varphi_b = 0$. We assumed that S_1 and S_3 are made of Al with $T_c = 1.4$ K. The normal-state resistances are $R_j = 2$ k Ω and $R_a = R_b = R_{\text{finger}} = 500$ Ω , whereas the volume of S_1 and S_2 are $\mathcal{V}_1 = 5 \times 10^{-20}$ m 3 and $\mathcal{V}_2 = 1 \times 10^{-19}$ m 3 , respectively. For completeness, in the thermal model we also included two pairs of superconducting probes tunnel-coupled to S_1 and S_2 acting as Josephson thermometers (see Sect. III) with a normal-state resistance $R_{\text{thermo}} = 2$ k Ω for each junction (not shown).

a few MHz,⁴¹ leading to fluctuations amplitudes of $\sim 10^{-13}$ W, i.e. at least one order of magnitudes less than the power scale needed to control the hysteresis of our thermal tunnel diode. This estimation is confirmed experimentally by Ref. 13, where the visibility of features with an amplitude of a few mK in the interference pattern generated by a Josephson heat modulator corresponds to a sensitivity of $10^{-14} \div 10^{-13}$ W in terms of electronic heat currents.

VI. ALTERNATIVE DESIGN OF THE HEAT TUNNEL DIODE

In this section, we briefly describe an alternative design of the tunnel heat diode, in which, as we shall show, the output temperature trend directly reflects the behavior of $J_{S_1S_2}$. The basic elements of the device are displayed in Fig. 5(a), where we can notice two main differences with respect to the

previous version of the tunnel diode. Firstly, S_2 is not completely thermalized at T_{bath} , but its electronic temperature T_2 is floating and can be measured as a function of the Joule power J_{in} injected in S_1 . Secondly, we added a normal-metal (N) electrode tunnel-coupled to S_2 acting as a cold finger, which permits to maintain a large temperature gradient between S_1 and S_2 . The electronic heat current flowing through the S_2 IN junction reads:¹

$$J_{\text{finger}}(T_2, T_{\text{bath}}) = \frac{2}{e^2 R_{\text{finger}}} \int_0^\infty \epsilon \mathcal{N}_2(\epsilon, T_2) [f(\epsilon, T_2) - f(\epsilon, T_{\text{bath}})] d\epsilon, \quad (12)$$

where R_{finger} is the normal-state resistance of the junction.

The thermal model used to predict the performance of the device is shown in Fig. 5(b), from which we obtain two energy-balance equations describing the thermal response of the system vs. J_{in} :

$$J_{\text{in}} = J_{S_1S_2}(T_1, T_2) + J_{SQUID}(T_1, T_{\text{bath}}) + J_{e-ph}(T_1, T_{\text{bath}}), \quad (13)$$

$$J_{S_1S_2}(T_1, T_2) = J_{\text{finger}}(T_2, T_{\text{bath}}) + J_{SQUID}(T_2, T_{\text{bath}}) + J_{e-ph}(T_2, T_{\text{bath}}). \quad (14)$$

The resulting behaviors of T_1 and T_2 can be seen in Figs. 5(c) and 5(d). Here, we chose S_1 and S_3 made of Al and we set $T_{\text{bath}} = 50$ mK, $\delta = 0.75$, $\varphi_j = \pi$, $\varphi_a = \varphi_b = 0$, $R_j = 2$ k Ω and $R_a = R_b = R_{\text{finger}} = 500$ Ω . We also assumed that S_1 and S_2 have volumes $\mathcal{V}_1 = 5 \times 10^{-20}$ m 3 and $\mathcal{V}_2 = 1 \times 10^{-19}$ m 3 , respectively. The calculated T_1 vs J_{in} is almost identical to the curve shown in Fig. 4(c), even though all the features appear less evident owing to the reduced thermal gradient $T_1 - T_2$, compared with the one obtained in the previous configuration. On the other hand, as T_1 increases, T_2 reaches a maximum and afterwards decreases until T_1 reaches T_{c1} . We emphasize that this behavior represents the direct proof of the NDTC effect, which generates a reduction of T_2 that can be as large as 80 mK and a region of thermal hysteresis that depends on the value of γ . It is therefore clear how this design, despite its slightly more complicated geometry and composition, might offer an indisputable direct evidence of NDTC and become an essential building block to realize a thermal transistor, as we shall argue in the next sections.

VII. THERMAL SWITCH AND MODULATOR

Once we have the ability to control electronic heat currents with NDTC, it is natural to exploit it in order to realize a thermal transistor. Similarly to its electronic analogue, the thermal transistor consists of three terminals: the source, the drain and the gate, residing at temperatures T_{source} , T_{drain} and T_{gate} , respectively. The last terminal is a control knob that can tune the thermal flow across the device, offering also the opportunity to obtain *heat amplification*. This is possible if the changes in the thermal current coming from the gate (J_{gate}) can induce an even larger change in the currents flowing from the source to the drain.^{2,17}

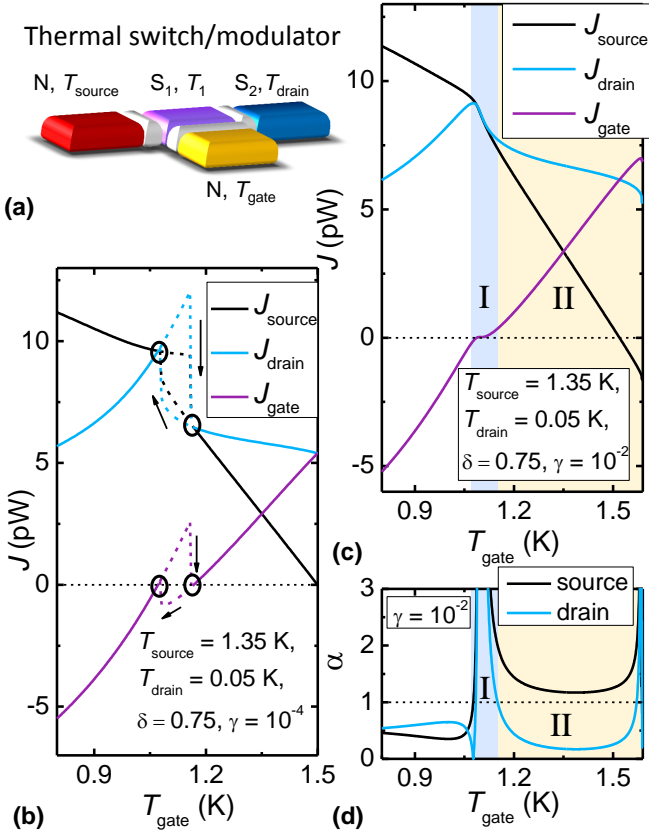


FIG. 6. Operation of a thermal switch and modulator. (a) Pictorial representation of the device. (b) Electronic heat currents J_{source} , J_{drain} and J_{gate} vs. T_{gate} for $\gamma = 10^{-4}$, $T_{\text{source}} = 1.35$ K, $T_{\text{drain}} = 50$ mK, $\delta = 0.75$, $R_{\text{source}} = 1$ k Ω , $R_{\text{gate}} = 1$ k Ω and $R_{\text{drain}} = 5.25$ k Ω . The arrows near the curves indicate the T_{gate} sweep direction, whereas the black circles indicate the stable working points of the thermal switch. (c) J_{source} , J_{drain} and J_{gate} vs. T_{gate} for the same parameters used in panel (b), except for $\gamma = 10^{-2}$ and $R_{\text{drain}} = 4.6$ k Ω . In panels (b) and (c) the horizontal dashed lines outline $J = 0$. (d) Amplification factors $\alpha_{\text{source,drain}}$ vs. T_{gate} for the same parameters chosen in panel (c). The horizontal dashed line indicates $\alpha = 1$. In panels (c) and (d), the shadowed regions I and II correspond to two different regimes of amplification (see text).

In order to envision the potential working operations of the transistor, we shall study two possible configurations of a three-terminal hybrid device. As shown in Fig. 6(a), in the first case two N electrodes play the roles of the source and the gate, while the central island and the drain consist in the S_1IS_2 junction that we analyzed in previous sections. In the following we will show that this structure can act as a thermal switch and modulator. On the other hand, if we connect a N gate to a S_1IS_2IN chain, we can obtain a thermal amplifier, as explained in the next section.

For simplicity, we set a fixed temperature gradient across the device, i.e. $T_{\text{source}} > T_{\text{drain}}$, and we assume that the device does not release energy to the environment. The latter hypothesis results to be accurate at low temperatures and for small volumes of the electrodes. Then, we analyze the behavior of the heat currents flowing out of the source and entering the

drain (J_{source} and J_{drain} , respectively) when we vary T_{gate} . This is obtained by solving the following energy-balance equation:

$$J_{\text{source}}(T_{\text{source}}, T_1) + J_{\text{gate}}(T_{\text{gate}}, T_1) = J_{\text{drain}}(T_1, T_{\text{drain}}), \quad (15)$$

where $J_{\text{source}} = (R_{\text{finger}}/R_{\text{source}})J_{\text{finger}}$, $J_{\text{drain}} = J_{S_1S_2}$ and $J_{\text{gate}} = (R_{\text{finger}}/R_{\text{gate}})J_{\text{finger}}$, while R_{source} , R_{gate} and R_{drain} are the normal-state resistances of the tunnel junctions connecting the central island to the other terminals of the device.

The results for $\gamma = 10^{-4}$ are shown in Fig. 6(b), where we set $T_{\text{source}} = 1.35$ K, $T_{\text{drain}} = 50$ mK, $\delta = 0.75$, $R_{\text{source}} = 1$ k Ω , $R_{\text{gate}} = 1$ k Ω and $R_{\text{drain}} = 5.25$ k Ω . We notice that $J_{\text{gate}} = 0$ at $T_{\text{gate}} = 1.07, 1.17$, pinpointing two stable working points where $J_{\text{source}} = J_{\text{drain}}$ [see the black circles in Fig. 6(b)]. These points can represent 1 and 0 Boolean states and do not depend on the history of the device. Therefore, our structure can work as a thermal switch.

Additionally, this system can operate as a thermal modulator, as displayed in Fig. 6(c) for the same parameters listed above except for $R_{\text{drain}} = 4.6$ k Ω and $\gamma = 10^{-2}$. The latter value has been chosen to suppress the thermal hysteresis [see Sect. V] and simplify the following analysis on heat amplification. As a matter of fact, even at a first glance, it is possible to note that the device can remarkably reduce J_{source} and J_{drain} in a region where J_{gate} remains close to zero [see region I in Fig. 6(c)]. This behavior can be evaluated more quantitatively by defining the amplification factor:¹⁷

$$\alpha_{\text{source,drain}} = \left| \frac{\partial J_{\text{source,drain}}}{\partial J_{\text{gate}}} \right| = \left| \frac{g_{\text{source,drain}}}{g_{\text{source}} + g_{\text{drain}}} \right|, \quad (16)$$

where we used Eq. (15) and defined $g_{\text{source}} = -\partial J_{\text{source}}/\partial T_1$ and $g_{\text{drain}} = \partial J_{\text{drain}}/\partial T_1$ as the differential thermal conductances of the source and drain tunnel junctions. From Eq. (16), it is clear that α can be > 1 only if one between g_{source} and g_{drain} is negative. In our case, the source is connected to the central island by means of the NIS₁ junction, which cannot show the NDTC effect and therefore we always have $g_{\text{source}} > 0$. Instead, the S_1IS_2 junction can generate $g_{\text{drain}} < 0$, as demonstrated in the previous sections.

The trend for α_{source} and α_{drain} vs. T_{gate} is shown in Fig. 6(d), where we can immediately distinguish two amplification regions I and II, shadowed in blue and yellow, respectively. In region I, i.e. for $1.08 \text{ K} \lesssim T_{\text{gate}} \lesssim 1.15 \text{ K}$, the performance of the thermal modulator is ideal and both the amplification factors are $\gg 1$. As shown in Fig. 6(c), this corresponds to the regime characterized by:

$$\frac{\partial J_{\text{gate}}}{\partial T_{\text{gate}}} = \frac{\partial T_1}{\partial T_{\text{gate}}}(g_{\text{source}} + g_{\text{drain}}) \sim 0, \quad (17)$$

where the identity between the first two sides has been obtained by using Eq. (15). Moreover, we have:

$$\frac{\partial T_1}{\partial T_{\text{gate}}} = -g_{\text{source}} \frac{\partial J_{\text{source}}}{\partial T_{\text{gate}}} > 0, \quad (18)$$

since $g_{\text{source}} > 0$ and $\partial J_{\text{source}}/\partial T_{\text{gate}}$ is negative in the whole range of operation [see Fig. 6(c)]. Thus, from Eq.(17) we obtain that region I is characterized by $g_{\text{source}} \sim -g_{\text{drain}}$ and

$\alpha_{\text{source,drain}} \gg 1$. Yet, in the whole extension of region II, i.e. $1.15 \text{ K} \lesssim T_{\text{gate}} \lesssim 1.59 \text{ K}$, the presence of the NDTC ($g_{\text{drain}} < 0$) still produces $\alpha_{\text{source}} > 1$, even though J_{gate} increases with a finite slope [see Fig. 6(c)].

This configuration would produce significant results also in a more realistic device that can release energy to the environment. As explained in the previous section, a N cold finger connected to S_2 would be able to maintain a relevant temperature gradient at the output of the transistor, leading to differences between the 1 and 0 states of the thermal switch exceeding 10 mK. Furthermore, it would be possible to obtain amplification factors > 1 by limiting the impact of the electron-phonon coupling with small volumes of the electrodes, especially for what concerns S_1 .

VIII. THERMAL AMPLIFIER

In this section, we briefly show the alternative configuration for a thermal transistor that can operate as a thermal *amplifier*. The structure is shown in Fig. 7(a) and consists of two N electrodes acting as the gate and the drain, while S_1 and S_2 embody the source and the central island, respectively. If we take the same assumptions described in the previous section, we can calculate J_{source} , J_{drain} and J_{gate} vs. T_{gate} , as displayed in Fig. 7(b) (see the caption for the detailed list of parameters). It is easy to observe that the electronic heat current curves present a very small region of thermal hysteresis, which cannot be used to realize an effective thermal switch. As anticipated in Sect. II, the effect is indeed reduced with respect to that observed in previous devices, since in this case the NDTC is obtained by varying T_2 instead of T_1 and is consequently much more localized in the proximity of the SMP. Nevertheless, if we consider a higher value of γ [see Fig. 7(c)], we can easily appreciate the amplification effect of our device. As we have noticed in the previous case, two different regimes I and II are visible [see Fig. 7(d)]: in region II, only α_{drain} is raised above 1 by the NDTC, while in region I ($\partial J_{\text{gate}}/\partial T_{\text{gate}} \simeq 0$ and both $\alpha_{\text{source,drain}} \gg 1$).

IX. CONCLUSIONS

In summary, we have analyzed the transport properties of a temperature-biased JJ composed by two different superconductors. From the point of view of charge transport, this S_1IS_2 junction can support a Josephson current, which present a remarkable jump when $\Delta_1(T_1) = \Delta_2(T_2)$. This feature has never been observed so far and would confirm the microscopic theory for a Josephson tunneling structure.^{26,30,34} Moreover, the temperature-dependence of the Josephson current could provide a valid alternative to probe the electronic temperature in superconducting electrodes.

Foremost, on the thermal side, a temperature gradient imposed across the S_1IS_2 junction can produce a sizable effect of NDTC, which exhibits a maximum peak-to-valley ratio $\simeq 3.1$ in the transmitted electronic heat current when the phase difference between the superconducting condensates is π . This

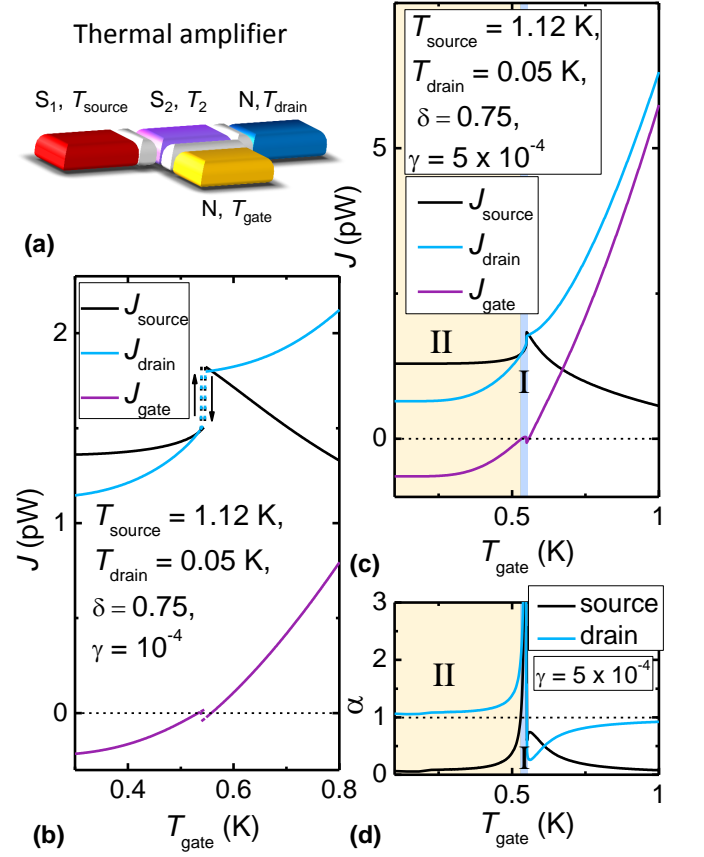


FIG. 7. Performance of a thermal amplifier. (a) Pictorial representation of the device. (b) Electronic heat currents J_{source} , J_{drain} and J_{gate} vs. T_{gate} for $\gamma = 10^{-4}$, $T_{\text{source}} = 1.12 \text{ K}$, $T_{\text{drain}} = 50 \text{ mK}$, $\delta = 0.75$, $R_{\text{source}} = 30 \text{ k}\Omega$, $R_{\text{gate}} = 5 \text{ k}\Omega$ and $R_{\text{drain}} = 1 \text{ k}\Omega$. The arrows near the curves indicate the T_{gate} sweep direction. (c) J_{source} , J_{drain} and J_{gate} vs. T_{gate} for the same parameters used in panel (b), except for $\gamma = 5 \times 10^{-4}$ and $R_{\text{gate}} = 1 \text{ k}\Omega$. In panels (b) and (c) the horizontal dashed lines outline $J = 0$. (d) Amplification factors $\alpha_{\text{source,drain}}$ vs. T_{gate} for the same parameters chosen in panel (c). The horizontal dashed line indicates $\alpha = 1$. In panels (c) and (d), the shadowed regions I and II correspond to two different regimes of amplification (see text).

requirement can be fulfilled with the help of a three-junction SQUID controlled by an external magnetic flux. With these elements, we envisioned two different designs for a thermal tunnel diode, which could immediately be implemented to observe a temperature modulation as large as 80 mK due to the NDTC effect. Under proper conditions, this device would also produce a thermal hysteresis that might serve to store information in a solid-state memory device at cryogenic temperatures.

Finally, we showed the potential applications of NDTC into two versions of a thermal transistor. In the first case, the device can act as a thermal switch and modulator, while in the second configuration our three-terminal structure operates as a thermal amplifier. In both the schemes we are able to obtain a remarkable heat amplification in a wide range ($\sim 500 \text{ mK}$) of the gate temperature. This result is a strict consequence of the NDTC, as predicted by Li *et al.*¹⁷

The proposed systems could be easily implemented by standard nanofabrication techniques and, combined with caloritronic interferometers^{10,12,13} and thermal diodes,⁶ might represent the last missing pieces to complete the thermal reproduction of the most important electronic devices. Besides being relevant from a fundamental physics point of view, these structures would find immediate technological application as essential building blocks in solid-state thermal nanocircuits and in general-purpose cryogenic electronic applications re-

quiring energy management.

We acknowledge the MIUR-FIRB2013–Project Coca (grant no. RBF1379UX), the European Research Council under the European Union’s Seventh Framework Programme (FP7/2007-2013)/ERC grant agreement no. 615187 - CO-MANCHE and the European Union (FP7/2007-2013)/REA grant agreement no. 630925 – COHEAT for partial financial support.

* antonio.fornieri@sns.it

† giazotto@sns.it

- ¹ F. Giazotto, T. T. Heikkilä, A. Luukanen, A. M. Savin, and J. P. Pekola, *Rev. Mod. Phys.* **78**, 217 (2006).
- ² N. Li, J. Ren, L. Wang, G. Zhang, P. Hänggi, and B. Li, *Rev. Mod. Phys.* **84**, 1045 (2012).
- ³ Y. Dubi and M. Di Ventra, *Rev. Mod. Phys.* **83**, 131 (2011).
- ⁴ O. Quaranta, P. Spathis, F. Beltram, and F. Giazotto, *Appl. Phys. Lett.* **98**, 032501 (2011).
- ⁵ J. T. Muhonen, M. Meschke, and J. Pekola, *Rep. Prog. Phys.* **75**, 046501 (2012).
- ⁶ M. J. Martínez-Pérez, A. Fornieri, and F. Giazotto, *Nat. Nanotechnol.* **10**, 303 (2015).
- ⁷ A. Fornieri, M. J. Martínez-Pérez, and F. Giazotto, *AIP Adv.* **5**, 053301 (2015).
- ⁸ M. A. Nielsen and I. L. Chuang, *Quantum Computation and Quantum Information* (Cambridge University Press, 2002).
- ⁹ S. Spilla, F. Hassler, and J. Splettstoesser, *New J. Phys.* **16**, 045020 (2014).
- ¹⁰ F. Giazotto and M. J. Martínez-Pérez, *Nature* **492**, 401 (2012).
- ¹¹ M. J. Martínez-Pérez, P. Solinas, and F. Giazotto, *J. Low Temp. Phys.* **175**, 813-837 (2014).
- ¹² M. J. Martínez-Pérez and F. Giazotto, *Nat. Commun.* **5**, 3579 (2014).
- ¹³ A. Fornieri, C. Blanc, R. Bosisio, S. D’Ambrosio, and F. Giazotto, *Nat. Nanotechnol.*, 10.1038/nnano.2015.281.
- ¹⁴ C. W. Chang, D. Okawa, A. Majumdar, and A. Zettl, *Science* **314**, 1121 (2006).
- ¹⁵ R. Xie, C. T. Bui, B. Varghese, Q. Zhang, C. H. Sow, B. Li, and J. T. L. Thong, *Adv. Funct. Mater.* **21**, 1602 (2011).
- ¹⁶ J. Bardeen and W. H. Brattain, *Phys. Rev.* **74**, 230 (1948).
- ¹⁷ B. Li, L. Wang, and G. Casati, *Appl. Phys. Lett.* **88**, 143501 (2006).
- ¹⁸ L. Esaki, *Phys. Rev.* **109**, 603 (1957).
- ¹⁹ R. C. Dynes, V. Narayanamurti, and J. P. Garno, *Phys. Rev. Lett.* **41**, 1509-1512 (1978).
- ²⁰ Tinkham, M. *Introduction to Superconductivity* (McGraw-Hill, 1996) and references therein.
- ²¹ K. Maki and A. Griffin, *Phys. Rev. Lett.* **15**, 921 (1965).
- ²² G. D. Guttman, B. Nathanson, E. Ben-Jacob, and D. J. Bergman, *Phys. Rev. B* **55**, 3849 (1997).
- ²³ E. Zhao, T. Löfwander, and J. A. Sauls, *Phys. Rev. Lett.* **91**, 077003 (2003).
- ²⁴ E. Zhao, T. Löfwander, and J. A. Sauls, *Phys. Rev. B* **69**, 134503 (2004).
- ²⁵ F. Giazotto and M. J. Martínez-Pérez, *Appl. Phys. Lett.* **101**, 102601 (2012).
- ²⁶ A. Barone and G. Paternò, *Physics and Applications of the Josephson Effect* (Wiley, New York, 1982).
- ²⁷ J. P. Pekola, T. T. Heikkilä, A. M. Savin, J. T. Flyktmann, F. Giazotto, and F. W. J. Hekking, *Phys. Rev. Lett.* **92**, 056804 (2004).
- ²⁸ J. P. Pekola, V. F. Maisi, S. Kafanov, N. Chekurov, A. Kemppinen, Yu. A. Pashkin, O.-P. Saira, M. Möttönen, and J. S. Tsai, *Phys. Rev. Lett.* **105**, 026803 (2010).
- ²⁹ B. D. Josephson, *Phys. Lett.* **1**, 251 (1962).
- ³⁰ E. R. Harris, *Phys. Rev. B* **10**, 84 (1974).
- ³¹ I. M. Pop, K. Geerlings, G. Catelani, R. J. Schoelkopf, L. I. Glazman, and M. H. Devoret, *Nature* **508**, 369 (2014).
- ³² F. Giazotto and J. P. Pekola, *J. Appl. Phys.* **97**, 023908 (2005).
- ³³ S. Tirelli, A. M. Savin, C. Pascual Garcia, J. P. Pekola, F. Beltram, and F. Giazotto, *Phys. Rev. Lett.* **101**, 077004 (2008).
- ³⁴ V. Ambegaokar and A. Baratoff, *Phys. Rev. Lett.* **10**, 486 (1963).
- ³⁵ A. V. Timofeev, C. Pascual Garcia, N. B. Kopnin, A. M. Savin, M. Meschke, F. Giazotto, and J. P. Pekola, *Phys. Rev. Lett.* **102**, 017003 (2009).
- ³⁶ M. J. Martínez-Pérez and F. Giazotto, *Appl. Phys. Lett.* **102**, 182602 (2013).
- ³⁷ F. C. Wellstood, C. Urbina, J. Clarke, *Phys. Rev. B* **49**, 5942, (1994).
- ³⁸ J. M. Martinis, G. C. Hilton, K. D. Irwin, and D. A. Wollman, *Nucl. Instr. Meth. Phys. Res. A* **444**, 23 (2000).
- ³⁹ G. Brammertz, A. A. Golubov, P. Verhoeve, R. den Hartog, A. Peacock, and H. Rogalla, *Appl. Phys. Lett.* **80**, 2955 (2002).
- ⁴⁰ D. Golubev, T. Faivre, and J. P. Pekola, *Phys. Rev. B* **87**, 094522 (2013).
- ⁴¹ J. P. Pekola, V. F. Maisi, S. Kafanov, N. Chekurov, A. Kemppinen, Yu. A. Pashkin, O.-P. Saira, M. Möttönen, and J. S. Tsai, *Phys. Rev. Lett.* **105**, 026803 (2010).